

Phonon-glass electron-crystal Behaviour by A site Disorder in n-Type Thermoelectric Oxides

Received 00th January 20xx,
Accepted 00th January 20xx

L. M. Daniels,^a S. N. Savvin,^a M. J. Pitcher,^a M. S. Dyer,^a J. B. Claridge,^a S. Ling,^b B. Slater,^b F. Cora,^b J. Alaria*^c and M. J. Rosseinsky*^a

DOI: 10.1039/x0xx00000x

www.rsc.org/

Oxide materials are of current interest as high-temperature energy-harvesting thermoelectrics in the automotive and manufacturing sectors due to their low cost, low toxicity and high chemical robustness. The phonon-glass electron crystal (PGE) concept which has been successfully used to optimise the thermoelectric figure of merit (ZT) in clathrates and skutterudites by combining the high electronic conduction of a crystal with the low thermal conduction of a glass is an approach which has not yet been realised in oxides due to the strong coupling between electronic and thermal transport. Through crystal chemistry engineering of the ABO_3 perovskite based around a combined experimental and computational understanding of the mechanisms responsible, PGE behaviour has been achieved for the first time in oxide thermoelectrics by decoupling thermal and electronic transport. By targeting the lattice component of the thermal conductivity (κ_{latt}), we have induced a glass-like κ_{latt} through the introduction of large mass disorder on the perovskite A site whilst retaining ABO_3 stoichiometry and avoiding vacancy defects that severely compromise electronic transport. Substitution at the perovskite B site with a donor cation allows for independent tuning of the electronic transport, producing a significant power factor. This high mass disorder approach will enable the PGE concept to be applied experimentally to a wide range of materials, and the computational results which support our observations can be used to generate descriptors towards theoretical screening of new high-performance PGE thermoelectrics.

Phonon-glass electron-crystal (PGE) behaviour is realised in $\text{La}_{0.5}\text{Na}_{0.5}\text{Ti}_{1-x}\text{Nb}_x\text{O}_3$ thermoelectric oxides. The vibrational disorder imposed by the presence of both La^{3+} and Na^+ cations on the A site of the ABO_3 perovskite oxide $\text{La}_{0.5}\text{Na}_{0.5}\text{TiO}_3$ produces a phonon-glass with a thermal conductivity, κ , 80% lower than that of SrTiO_3 at room temperature. Unlike other state-of-the-art thermoelectric oxides, where there is strong coupling of κ to the electronic power factor, the electronic transport of these materials can be optimised independently of the thermal transport through cation substitution at the octahedral B site. The low κ of the phonon-glass parent is retained across the $\text{La}_{0.5}\text{Na}_{0.5}\text{Ti}_{1-x}\text{Nb}_x\text{O}_3$ series without disrupting the electronic conductivity, affording PGE behaviour in oxides.

Thermoelectric generators offer enhanced energy efficiency across the industrial and automotive sectors through the conversion of waste heat into electricity. Materials performance is assessed by the dimensionless figure of merit $ZT = (S^2\sigma/\kappa)T$, combining the

thermal conductivity (κ), absolute temperature (T), the Seebeck coefficient (S) and electrical conductivity (σ), which together define the power factor ($S^2\sigma$). One strategy to optimise ZT is the phonon-glass electron-crystal (PGE) concept proposed by Slack,¹ which aims to decouple the quantities governed by the Boltzmann transport equation in an “electron-crystal”, by maximising S and σ , from the quantity governed by phonon transport processes in a “phonon-glass” (PG) by minimising the lattice contribution to the thermal conductivity (κ_{latt}); essentially, a crystal that transports charge like a semiconductor, whilst hindering the transport of heat by the lattice like a glass.² Heat transport in solids consists of lattice and electronic (κ_{elec}) contributions through $\kappa = \kappa_{\text{latt}} + \kappa_{\text{elec}}$, and $\kappa_{\text{latt}} = 1/3C_v l_{\text{ph}} v_s$ (Equation 1), where C_v is the isochoric heat capacity, l_{ph} the average phonon mean free path (MFP), and v_s the mean velocity of sound. Different heat-carrying mechanisms lead to a broad distribution of MFPs, ranging from the atomic scale (<1 nm) for point defect scattering, to the mesoscale (>100 nm) for grain boundary scattering. In a “phonon-crystal” (PC), heat is transported by phonons of well-defined wavelength. The phonon scattering rate (τ_{ph}^{-1}), which is inversely proportional to κ_{latt} (Equation S1, ESI[†]), corresponds to the sum of the inverse relaxation times of several phonon-scattering mechanisms that contribute separately to κ and is described quantitatively by the modified Debye-Callaway model (Equation S3, ESI[†]).³ This produces a T^{-1} temperature dependence of κ above the Debye temperature (θ_b) where heat conduction is by

^a Department of Chemistry, University of Liverpool, Crown Street, Liverpool, L69 7ZD, United Kingdom. Email: m.j.rosseinsky@liverpool.ac.uk

^b Department of Chemistry, University College London, Gower Street, London, WC1E 6BT, United Kingdom.

^c Department of Physics, University of Liverpool, Oxford Street, Liverpool, L69 7ZE, United Kingdom. Email: jonathan.alaria@liverpool.ac.uk

† Electronic Supplementary Information (ESI) available. See DOI: 10.1039/x0xx00000x

acoustic phonons interacting through anharmonic phonon-phonon Umklapp processes (Equation S6, ESI[†]) that is characteristic of PCs. The identification of the phonon-scattering processes that limit heat conduction in a material has led to a panoscopic approach to reduce κ for PC materials.^{4, 5} Here κ remains above the minimum thermal conductivity (κ_{\min}) expected for a PG, where the thermal conductivity is described by a coupled lattice of harmonic oscillators vibrating with the same frequency but with random phases, and κ_{\min} can be calculated using Cahill's model (Equation S9, ESI[†]) from the number density of atoms (N) and θ_b .⁶ The phonon MFP of a PG is much smaller than a PC and remains constant as a function of temperature as all vibrations are localised over interatomic distances. Through Equation 1, κ_{latt} of a PG exhibits a characteristic temperature dependence which follows the heat capacity above θ_b , in contrast to $\kappa(T)$ of a PC which asymptotically approaches this lower PG κ_{\min} limit from above at high temperature. PG behaviour of κ was observed in amorphous and disordered insulating materials,^{7, 8} and realised in high performance thermoelectrics such as skutterudites and clathrates which behave as PGECs through the incorporation of "rattling" effects produced by extensive low-frequency ion displacements within large cages in the framework structures of these systems.^{9, 10} Recently, ultralow thermal conductivities of 0.4–0.5 Wm⁻¹K⁻¹ resulting from bonding anharmonicity where weakly bound cations act as rattlers were observed in metal tellurides.^{11, 12}

As part of the search for materials based on less toxic and/or scarce components^{13, 14} that can operate under more demanding conditions including the broad temperature ranges required for some applications (automotive exhaust waste heat recovery: 350–700 K, industrial furnace waste heat recovery: 700–1100 K),^{15, 16} there is growing interest in thermoelectric oxides.^{17, 18} However, the strategies used to design high-performance thermoelectric materials based on small band gap, broad-band semiconductors and intermetallics cannot be translated directly to oxide materials.¹⁹ Transition metal oxides are often narrow-band semiconductors with electronic transport properties that are not governed by the Boltzmann equation, and typically have poor mobilities and conductivities compared to classical semiconductors. Therefore, considerable effort has been focused on finding oxide materials with large power factors by optimising σ and S , which has led to reasonably high performance in p-type layered cobaltate oxides, Ca₃Co₄O₉ and Na_xCoO₂, with ZT values of ≈ 0.4 and ≈ 0.6 at 700 K, respectively.^{20, 21} Both p- and n-type semiconductors are needed for device fabrication, and it has been more difficult to achieve comparable performance in n-type oxides. By exploiting the band structure of the perovskite oxide SrTiO₃ (STO), which has contributions from both light and heavy electrons at the Fermi level,²² it is possible to achieve large power factors of 28–36 $\mu\text{WK}^{-2}\text{cm}^{-1}$ at 300 K in n-type Sr_{1-x}La_xTiO_{3- δ} ($x = 0.015$ – 0.1) single crystals, however, the performance is negated by the large κ of ≈ 12 Wm⁻¹K⁻¹.²³ The nanostructuring approaches used to reduce κ in classical compound semiconductors and intermetallics by increasing grain boundary scattering are inefficient in titanate perovskites as the phonon MFP of SrTiO₃ is 2–3 nm, requiring nanometer-sized grains for any noticeable effect on κ .^{4, 24} Because of this inherently small phonon MFP, the best strategy to reduce κ_{latt} is through the introduction of point defect scattering achieved by substitution. The

scattering time for point defects (τ_{PD}) is added to the other scattering processes according to the Mathiessen rule,²⁵ and is influenced heavily by the disorder scattering parameter, $\Gamma = \Gamma_{\text{MF}} + \Gamma_{\text{SF}}$, where Γ_{MF} is the mass fluctuation arising from the mass contrast introduced by the defect and Γ_{SF} the strain field induced by ionic radius variance of the defect (Equation S5, ESI[†]). Calculation of Γ predicts the effect of substitution on κ , and the calculated contributions to Γ for several previously-reported titanate perovskites, substituted with different rare-earth cations and/or vacancies, are given in Table 1.

A 57% decrease in κ from that of STO is observed at 700 K in the experimental data presented in Fig. 1a upon the introduction of 10% of Dy³⁺ on the A site in Sr_{0.9}Dy_{0.1}TiO_{3- δ} (SDTO). Using measured and calculated, rather than fitted, parameters (Table S1, ESI[†]), $\kappa(T)$ of both materials is well described by the Debye–Callaway model.³ In particular, the addition of the calculated point defect scattering for SDTO in Table 1 results in a good agreement with the data in contrast to the previous study for Sr_{0.9}Y_{0.1}TiO_{3- δ} (Table 1) where a discrepancy between calculated and fitted Γ_{SF} was observed.²⁶ The effect of this disorder on the AO₃ network phonons is represented qualitatively as a spring model in Fig. 1b, c, which emphasises the retained periodicity of the force constants in SDTO, with substantial enhancement of Γ achieved via substitutional disorder as a perturbation of the ordered array. The observation of a transition from PC to PG behaviour in the Sr_{1-x}La_{0.67x}□_{0.33x}TiO₃ system when the A site cation vacancy (□) content exceeded 20% ($x=0.6$), significantly increasing Γ_{MF} (Table 1) and resulting in a κ close to κ_{\min} from Cahill's model, was rather encouraging.²⁷ However, the complex defect chemistry of these materials did not allow for electronic doping whilst simultaneously retaining the PG behaviour, as compositions with carrier concentrations sufficient for good thermoelectric response displayed PC thermal conductivity. In order to realise PGEC behaviour in titanates, a strategy is required that combines an equivalent Γ to those achieved by cation vacancy-containing materials with a structural chemistry that permits electronic doping.

Table 1 Calculated dimensionless disorder scattering parameters (Γ), including mass fluctuation (Γ_{MF}) and strain field (Γ_{SF}) terms, for reported doped titanate perovskites. The nature (phonon-glass or –crystal) of the heat transport are shown.

Material	Γ	Γ_{MF}	Γ_{SF}	State
Sr _{0.9} Y _{0.1} TiO _{3-δ} ²⁶	3.02×10^{-3}	1.93×10^{-5}	3.00×10^{-3}	PC
Sr _{0.9} Dy _{0.1} TiO _{3-δ} ²⁸	5.59×10^{-2}	5.58×10^{-2}	2.80×10^{-3}	PC
Sr _{1-x} La _{0.67x} □ _{0.33x} TiO ₃ , $x=0.4$ ²⁷	0.213	0.212	5.92×10^{-4}	PC
Sr _{1-x} La _{0.67x} □ _{0.33x} TiO ₃ , $x=0.8$ ²⁷	0.405	0.404	4.88×10^{-4}	PG
Nd _{0.67-x} Li _{3x} □ _{0.33-2x} TiO ₃ ²⁹	0.701	0.694	6.84×10^{-3}	PG

The A site substitution of two Sr²⁺ cations in STO for the charge-balancing cation pair La³⁺ and Na⁺ preserves the overall stoichiometry of the parent structure,³⁰ while introducing charge, size and mass disorder. Structural characterisation of La_{0.5}Na_{0.5}TiO₃ (LNTO) with synchrotron powder X-ray and neutron diffraction gave good agreement with the reported rhombohedral structure (Fig. S1, Table S2, ESI[†]),³¹ most importantly highlighting that La³⁺ and Na⁺ are fully disordered on the A site. Despite this, the anisotropic displacement parameters do not indicate a strong local deviation away from the average structure with a root mean square displacement of 0.078(9) Å for the A site at 300 K, showing that

LNTO is a crystalline solid with disordered A site cation distribution. The incorporation of both La^{3+} and Na^{+} on the A site in LNTO achieves a higher Γ (0.513) than that observed for PG $\text{Sr}_{1-x}\text{La}_{0.67x}\text{Ti}_{0.33x}\text{TiO}_3$ where $x = 0.8$, with Γ_{MF} contributing 99.9% of this value. Both STO and LNTO measured in this study are electronically insulating with $\sigma < 3 \times 10^{-12} \text{ S cm}^{-1}$ at 300 K, thus κ corresponds to κ_{latt} . The thermal conductivity of LNTO ($2.29 \pm 0.12 \text{ W m}^{-1} \text{ K}^{-1}$ at 700

the maximum value permitted from the size of the cell used for the calculations, confirming the “delocalised” nature of the phonons. In the case of LNTO, a 20% decrease in d_{average} is observed that suggests increased phonon localisation in the disordered crystal. The random distribution of high mass-contrast La^{3+} and Na^{+} cations can be envisaged as producing locally decoupled oscillators with dramatically different vibrational frequencies (Fig. 1e), which

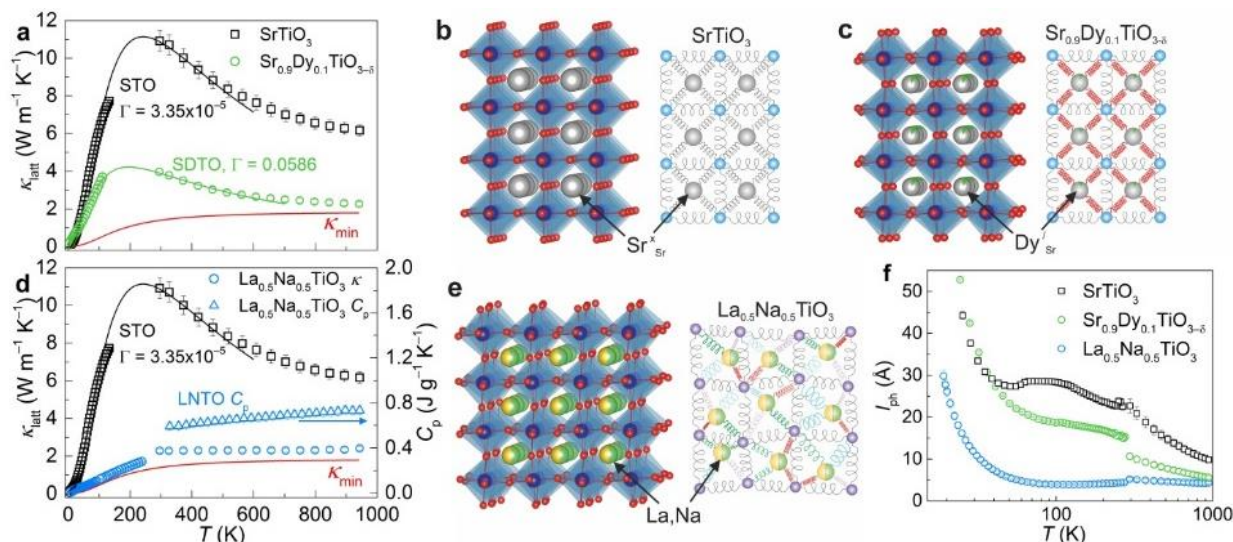


Fig. 1 Measured κ_{latt} for phonon-crystals SrTiO_3 and $\text{Sr}_{0.9}\text{Dy}_{0.1}\text{TiO}_{3-6}$ are shown in a) and are compared against the Debye-Callaway model for crystalline solids (solid lines),³ alongside example spring models b) and c), illustrating phonon coupling between nearest-neighbours in the crystal structure with identical force constants. The theoretical κ_{min} of STO is calculated from Cahill's model for disordered crystalline solids,⁶ and is compared against the experimental data in a) and d). The κ_{latt} of $\text{La}_{0.5}\text{Na}_{0.5}\text{TiO}_3$ (LNTO) shown in d) cannot be modelled as a phonon-crystal using the Callaway model, and compares much more closely to κ_{min} of a phonon-glass, with a temperature dependence that follows the contribution of the heat capacity (C_p) shown on the right-hand axis of d). The vibrational disorder of LNTO resulting from phonon interactions between randomly distributed A site cations with high mass contrast and the rest of the structure is illustrated through the spring model in e). Phonon mean free paths shown in f) are extracted using the measured κ_{latt} , C_p , and speed of sound v_s in Equation 1, where v_s is calculated from Equation 2 using θ_b obtained by fitting C_p data. Error bars representing the uncertainty in numerical values in a), d) and f) are smaller than the symbols except for the high-temperature κ_{latt} and l_{ph} for STO.

K) is dramatically reduced by 66 % from that of STO ($6.83 \pm 0.35 \text{ W m}^{-1} \text{ K}^{-1}$ at 700 K) in Fig. 1d, and follows the temperature dependence of the heat capacity, a distinguishing feature of a PG. As a result it is not possible to use the Debye-Callaway model for PCs to describe the evolution of $\kappa(T)$ of LNTO. Instead, both the magnitude and temperature dependence of κ compare closely to the κ_{min} expected for STO if it displayed PG heat transport, calculated with the Cahill model (Equation S9, ESI[†]), using the cut-off frequencies θ_i calculated from the measured longitudinal and transverse velocities of sound for STO crystals.³² Despite the crystalline nature of LNTO, at high temperature the heat transport is no longer mediated by coherent and long-distance propagation of phonons through the lattice, but rather occurs via hops of elementary lattice excitations in a diffusional manner. Spectral phonon analysis on the low temperature thermal conductivity shows that the dominant scattering mechanism is due to the point defects introduced by the increased A site charge and mass disorder (Fig. S2, ESI[†]).

To confirm this concept, we have performed phonon calculations for STO and LNTO at density functional theory (DFT) level using the finite-displacement method (ESI[†]). We also computed the average separation (d_{average}) between the 10 atoms exhibiting the largest phonon displacement amplitudes for each individual phonon mode across the spectrum (Fig. 2a). This quantity is a qualitative indicator of the phonon “localisation” (inset of Fig. 2a). The d_{average} of STO across the spectrum is close to 11 Å, which is

efficiently disrupt the coherent phonon transport that was

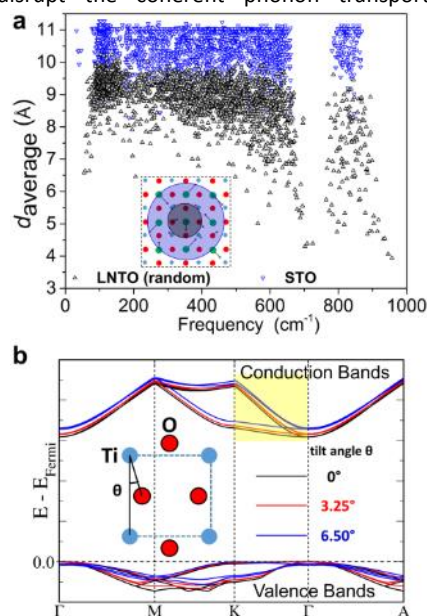


Fig. 2. Localisation of phonons a) in STO (blue, downward triangle) and LNTO (black, upward triangle) from static DFT calculations; for each individual phonon mode, d_{average} is calculated as the mean distance between the 10 atoms that participate to the greatest extent in a given phonon mode as defined by their displacement amplitudes. The schematic inset illustrates a localised (black circle) and a delocalised (blue circle) phonon mode. b) Energy dispersion of selected electronic bands at the band edges of undoped STO (in a rhombohedral cell with $R3c$ space group symmetry) with different degrees of octahedral tilting θ (see the inset for definition of tilt angle). All the bands have been aligned to the Fermi level, and the splitting of the t_{2g} states at the bottom of the conduction band into dispersive and dispersion-less bands is highlighted in yellow. The full band structure of cubic STO (with zero tilting) is shown in Fig. S17, ESI[†].

previously well-established by the periodic nearest-neighbour couplings in STO (Fig. 1b). As a result of this vibrational glassiness, the phonon MFP of ≈ 5 Å for LNTO (evaluated with Equation 1 from the measured heat capacity, lattice thermal conductivity and mean velocity of sound $v_s = \theta_D k_B / \hbar \sqrt{6\pi^2 N}$ (Equation 2)), where $\theta_D = 605$ K is extracted from the heat capacity (Fig. S3, Table S3, ESI[†]) remains constant over a wide temperature range (Fig. 1f) from 80K to 1000K. Glass-like thermal conductivity is established in $\text{La}_{0.5}\text{Na}_{0.5}\text{TiO}_3$ through phonon engineering by utilising mass, size and charge disorder of the A site cations.

This complete A site replacement of Sr^{2+} with La^{3+} and Na^+ in $\text{La}_{0.5}\text{Na}_{0.5}\text{TiO}_3$ retains the flexible B site substitution chemistry of STO, and allows the introduction of electronic dopant cations into PG LNTO to produce a significant power factor. Synthesis of $\text{La}_{0.5}\text{Na}_{0.5}\text{Ti}_{1-x}\text{Nb}_x\text{O}_3$ at 1623 K under H_2/N_2 (5%) atmosphere utilising sacrificial powder to prevent the loss of sodium from cold-pressed pellets afforded substitution of Nb^{5+} in phase pure materials to $x = 0.2$ (Fig. S4, ESI[†]). The unit cell parameters increase with x (Fig. 3a) consistent with substitution of Nb^{5+} forming Ti^{3+} , both of which are larger than Ti^{4+} ($r_{\text{Nb}^{5+}} = 0.64$ Å, $r_{\text{Ti}^{3+}} = 0.67$ Å and $r_{\text{Ti}^{4+}} = 0.605$ Å).³³ The octahedral tilt angle, ϕ ,³⁴ decreases from $7.9142(7)^\circ$ at $x = 0$ to $7.2219(18)^\circ$ for $x = 0.2$ (Fig. S5, Table S5, ESI[†]) as the structure tends more towards cubic symmetry with increasing x , and both the mean B–O and A–O distances increase following the expansion of the unit cell. The distortion observed in the crystal structure of LNTO compared to STO could be detrimental to the achievement of a high power factor, due to a change of band dispersion with octahedral tilt angle (Fig. 2b). However, by calculating the electronic structure of STO for different tilt angles (ESI[†]) we found that the coexistence of dispersive and dispersion-less bands at the bottom of the conduction band is retained for the range of tilt angles observed in the Nb-doped LNTO series, and the ratio of effective electronic mass for the two bands remains ≈ 5 for all tilt angles examined, which is similar to the values reported for cubic STO previously.²² Tauc plots from diffuse reflectance data show that the parent and doped compositions of LNTO have band gaps of ≈ 3.2 eV, which is similar to STO (Fig. S8, Table S9, ESI[†]). The electronic conductivity at 500 K increases as a function of x in $\text{La}_{0.5}\text{Na}_{0.5}\text{Ti}_{1-x}\text{Nb}_x\text{O}_3$ from $\sigma = 120 \pm 6$ S cm^{-1} at $x = 0.05$ to 360 ± 18 S cm^{-1} at $x = 0.2$ (Fig. 3b). This is consistent with the linear increase of the carrier concentrations (from 7×10^{20} cm^{-3} for $x=0.05$ to 3.2×10^{21} cm^{-3} for $x=0.2$) obtained from the temperature dependence of the Seebeck coefficient and a mobility ≈ 1 $\text{cm}^2 \text{V}^{-1} \text{s}^{-1}$ (Fig. S9, Table S4, ESI[†]). The increase in σ with T below 500 K is ascribed to the formation of resistive depletion layers of acceptor-based dopants segregated to the grain boundaries (Fig. S9, ESI[†]).³⁵ Above this temperature, σ decreases with increasing T as carrier mobility is reduced with a σ for $\text{La}_{0.5}\text{Na}_{0.5}\text{Ti}_{0.8}\text{Nb}_{0.2}\text{O}_3$ comparable to that of $\text{Sr}_{0.9}\text{Dy}_{0.1}\text{TiO}_{3-\delta}$ measured in this study. Observation of negative thermopowers indicates that the carriers are predominantly n-type in nature, and the absolute magnitudes of $S_{500\text{K}}$ decrease from -222 ± 11 to -127 ± 6 $\mu\text{V K}^{-1}$ from $x = 0.05$ to 0.2 as a result of increasing carrier concentration n (Fig. 3c). The observed magnitudes and temperature dependencies exhibited by both σ and S (Fig. S9, ESI[†]) are comparable to many of the titanates reported previously, which were doped on either the A or B sites.^{27, 28, 36, 37} The observation of high S and σ suggests that the unique band structure of STO,

consisting of heavy and light electrons, that allows for high power factors is retained in $\text{La}_{0.5}\text{Na}_{0.5}\text{Ti}_{1-x}\text{Nb}_x\text{O}_3$ despite the slight distortion of the structure away from cubic symmetry, consistent with the DFT calculations. A maximum power factor of 0.62 ± 0.07 $\text{mW m}^{-1} \text{K}^{-2}$ was obtained for $\text{La}_{0.5}\text{Na}_{0.5}\text{Ti}_{0.8}\text{Nb}_{0.2}\text{O}_3$ at ≈ 700 K (Fig. S10, ESI[†]). A linear dependence of power factor upon x is observed at 900 K which is different to other Nb-doped titanates, where peak

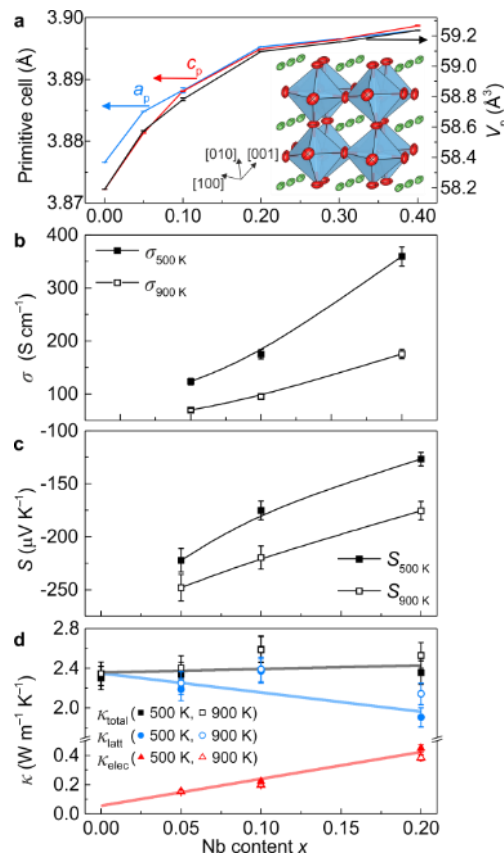


Fig. 3 Variation of primitive unit cell parameters and volume as a function of x in $\text{La}_{0.5}\text{Na}_{0.5}\text{Ti}_{1-x}\text{Nb}_x\text{O}_3$. a). Pseudocubic representation of $\text{La}_{0.5}\text{Na}_{0.5}\text{TiO}_3$ with anisotropic displacement parameters for the A and O sites is included, highlighting the well-defined crystallographic positions of the A site cations. Atom colours: A site green, B site blue, O red. Dependence of σ and S upon x is shown in b) and c). The dependence of κ , κ_{latt} , and κ_{elec} upon x is shown in d), reflecting the PGEC behaviour of $\text{La}_{0.5}\text{Na}_{0.5}\text{Ti}_{1-x}\text{Nb}_x\text{O}_3$.

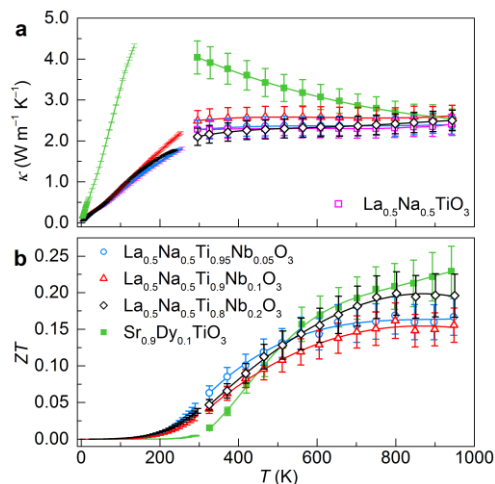


Fig. 4 Temperature dependence of a) κ for $\text{La}_{0.5}\text{Na}_{0.5}\text{Ti}_{1-x}\text{Nb}_x\text{O}_3$ compositions ($x = 0-0.2$) showing retention of a PG $\kappa(T)$ even after electronic substitution with Nb^{5+} ; and b) figure of merit ZT . Data measured from $\text{Sr}_{0.9}\text{Dy}_{0.1}\text{TiO}_{3-\delta}$ are included for comparison purposes.

values are typically achieved at $x \approx 0.1$. In contrast to the strong doping dependence of σ and S (Fig. 3b and 3c), the magnitudes of total thermal conductivity (κ_{total}), in the range of 2.34 ± 0.12 – $2.59 \pm 0.13 \text{ W m}^{-1} \text{ K}^{-1}$, are only 2 to 10% higher than undoped $\text{La}_{0.5}\text{Na}_{0.5}\text{TiO}_3$ and thus almost independent of B site substitution (Fig. 3d). All of the electronically-conducting $\text{La}_{0.5}\text{Na}_{0.5}\text{Ti}_{1-x}\text{Nb}_x\text{O}_3$ compositions exhibit the same glass-like temperature dependence of κ that was observed for LNTO, meaning that $\kappa_{300\text{K}} \approx \kappa_{900\text{K}}$ for all x (Fig. 4a). The lattice contribution to the thermal conductivity (κ_{latt}) decreases as the electronic contribution (κ_{elec}) increases from 6.5 at $x = 0.05$ to 19% at $x = 0.2$ at 500 K (Fig. 3d, Fig. S11, ESI[†]). The retention of PG temperature dependences and magnitudes of κ in electronically-conducting $\text{La}_{0.5}\text{Na}_{0.5}\text{Ti}_{1-x}\text{Nb}_x\text{O}_3$ (Fig. 4a) reflects decoupling of thermal and electronic transport, which has not previously been reported in an oxide thermoelectric family.

The $\text{La}_{0.5}\text{Na}_{0.5}\text{Ti}_{1-x}\text{Nb}_x\text{O}_3$ compositions produce ZT temperature dependences with peak values around 0.2 above 900 K (Fig. 4b) which are comparable with the values obtained for $\text{Sr}_{0.9}\text{Dy}_{0.1}\text{TiO}_{3-\delta}$ in this study. The increase in σ and reduction of κ in the intermediate temperature range (400–800 K) for PGEC $\text{La}_{0.5}\text{Na}_{0.5}\text{Ti}_{1-x}\text{Nb}_x\text{O}_3$ results in an improved ZT over SDTO up to 550 K. As a result, the average energy-conversion efficiencies (ϵ_{ave} , Equation 3) of the new PGEC $\text{La}_{0.5}\text{Na}_{0.5}\text{Ti}_{1-x}\text{Nb}_x\text{O}_3$ materials (1.93%) are slightly higher than $\text{Sr}_{0.9}\text{Dy}_{0.1}\text{TiO}_{3-\delta}$ (1.91%):

$$\epsilon_{\text{ave}} = \frac{\frac{T_{\text{H}} - T_{\text{C}}}{T_{\text{H}}} \int_{T_{\text{C}}}^{T_{\text{H}}} \frac{\sqrt{ZT+1}-1}{\sqrt{ZT+1}+(T_{\text{C}}/T_{\text{H}})} dT}{T_{\text{H}} - T_{\text{C}}} \quad (3)$$

where T_{H} and T_{C} are the hot- and cold-end temperatures of the material, and are set to 700 and 350 K, respectively, temperatures which are applicable to automotive exhaust waste heat recovery.¹⁶

Conclusions

Phonon engineering of SrTiO_3 by complete substitution of the A site cations to enhance charge and mass disorder in $\text{La}_{0.5}\text{Na}_{0.5}\text{TiO}_3$ produces an 80% reduction of the thermal conductivity which has the temperature dependence of a PG. The glass-like thermal conductivity is retained upon B site substitution with the donor Nb^{5+} , which enhances electronic transport to afford a PGEC oxide thermoelectric. By fixing the disordered A site composition to achieve the glassy κ , it is possible to independently tune the carrier concentration via B site chemistry analogous to that established in STO itself, allowing decoupling of the usually strongly covarying thermal and electronic transport properties. It is worthwhile to note that such substitutions may control thermal conductivity across a range of current thermoelectrics, and should be considered as a route to improving ZT further.

Acknowledgements

We thank EPSRC for funding under EP/N004884. We thank Diamond Light Source and ISIS for provision of beamtime and Chiu Tang, Claire Murray, and Alexandra Gibbs for assistance on the I11 and HRPD instruments. Troy Manning is thanked for his assistance with diffuse reflectance measurements.

Notes and references

- G. A. Slack, *CRC Handbook of Thermoelectrics*, CRC, Boca Raton, 1995.
- M. Beekman, D. T. Morelli and G. S. Nolas, *Nat. Mater.*, 2015, **14**, 1182–1185.
- J. Callaway, *Phys. Rev.*, 1959, **113**, 1046–1051.
- G. Tan, L. D. Zhao and M. G. Kanatzidis, *Chem Rev*, 2016, **116**, 12123–12149.
- T. Zhu, Y. Liu, C. Fu, J. P. Heremans, J. G. Snyder and X. Zhao, *Adv. Mater.*, 2017, **29**, 1605884.
- D. G. Cahill, S. K. Watson and R. O. Pohl, *Phys. Rev. B*, 1992, **46**, 6131–6140.
- D. G. Cahill and R. O. Pohl, *Ann. Rev. Phys. Chem.*, 1988, **39**, 93–121.
- M. D. Nielsen, V. Ozolins and J. P. Heremans, *Energy Environ. Sci.*, 2013, **6**, 570–578.
- M. Christensen, A. B. Abrahamsen, N. B. Christensen, F. Juranyi, N. H. Andersen, K. Lefmann, J. Andreasson, C. R. Bahl and B. B. Iversen, *Nat. Mater.*, 2008, **7**, 811–815.
- M. M. Koza, M. R. Johnson, R. Viennois, H. Mutka, L. Girard and D. Ravot, *Nat. Mater.*, 2008, **7**, 805–810.
- M. K. Jana, K. Pal, U. V. Waghmare and K. Biswas, *Angew. Chem. Int. Ed.*, 2016, **55**, 7792–7796.
- M. K. Jana, K. Pal, A. Warankar, P. Mandal, U. V. Waghmare and K. Biswas, *J. Am. Chem. Soc.*, 2017, **139**, 4350–4353.
- M. W. Gaultois, T. D. Sparks, C. K. H. Borg, R. Seshadri, W. D. Bonificio and D. R. Clarke, *Chem. Mater.*, 2013, **25**, 2911–2920.
- S. Hebert, D. Berthebaud, R. Daou, Y. Breard, D. Pelloquin, E. Guilmeau, F. Gascoin, O. Lebedev and A. Maignan, *J Phys Condens Matter*, 2016, **28**, 013001.
- S. LeBlanc, S. K. Yee, M. L. Scullin, C. Dames and K. E. Goodson, *Renewable Sustainable Energy Rev.*, 2014, **32**, 313–327.
- J. Yang and T. Caillat, *MRS Bull.*, 2011, **31**, 224–229.
- J. W. Fergus, *J. Eur. Ceram. Soc.*, 2012, **32**, 525–540.
- K. Koumoto, R. Funahashi, E. Guilmeau, Y. Miyazaki, A. Weidenkaff, Y. Wang, C. Wan and X. D. Zhou, *J. Am. Ceram. Soc.*, 2013, **96**, 1–23.
- E. Rausch, B. Balke, J. M. Stahlhofen, S. Ouardi, U. Burkhardt and C. Felser, *J. Mater. Chem. C*, 2015, **3**, 10409–10414.
- K. Fujita, T. Mochida and K. Nakamura, *Jpn. J. Appl. Phys.*, 2001, **40**, 4644–4647.
- M. Shikano and R. Funahashi, *Appl. Phys. Lett.*, 2003, **82**, 1851–1853.
- K. Shirai and K. Yamanaka, *J. Appl. Phys.*, 2013, **113**, 053705.
- T. Okuda, K. Nakanishi, S. Miyasaka and Y. Tokura, *Phys. Rev. B*, 2001, **63**.
- Y. Wang, K. Fujinami, R. Zhang, C. Wan, N. Wang, Y. Ba and K. Koumoto, *Appl. Phys. Express*, 2010, **3**, 031101.
- T. M. Tritt, *Thermal Conductivity: Theory, Properties and Applications*, Kluwer Academic, New York, USA, 2004.
- S. Bhattacharya, A. Mehdizadeh Dehkordi, S. Tennakoon, R. Adebisi, J. R. Gladden, T. Darroudi, H. N. Alshareef and T. M. Tritt, *J. Appl. Phys.*, 2014, **115**, 223712.
- S. R. Popuri, A. J. M. Scott, R. A. Downie, M. A. Hall, E. Suard, R. Decourt, M. Pollet and J. W. G. Bos, *RSC Adv.*, 2014, **4**, 33720–33723.
- A. V. Kovalevsky, A. A. Yaremchenko, S. Populoh, P. Thiel, D. P. Fagg, A. Weidenkaff and J. R. Frade, *Phys. Chem. Chem. Phys.*, 2014, **16**, 26946–26954.
- Y. Ba, C. Wan, Y. Wang, W. Norimatsu, M. Kusunoki and K. Koumoto, *Mater. Lett.*, 2013, **97**, 191–194.

- 30 R. Ranjan, A. Senyshyn, H. Boysen, C. Baehtz and F. Frey, *J. Solid State Chem.*, 2007, **180**, 995-1001.
- 31 R. Garg, A. Senyshyn, H. Boysen and R. Ranjan, *J. Phys.: Condens. Matter*, 2008, **20**, 505215.
- 32 W. Kaiser and R. Zurek, *Phys. Lett.*, 1966, **23**, 668.
- 33 R. D. Shannon, *Acta Cryst. A*, 1976, **32**, 751-767.
- 34 H. D. Megaw and C. N. W. Darlington, *Acta Cryst. A*, 1975, **31**, 161-173.
- 35 R. Moos and K. H. Härdtl, *J. Appl. Phys.*, 1996, **80**, 393-400.
- 36 T. Q. Thong, L. T. T. Huong and N. T. Tinh, *Mater. Trans.*, 2015, **56**, 1365-1369.
- 37 B. Zhang, J. Wang, T. Zou, S. Zhang, X. Yaer, N. Ding, C. Liu, L. Miao, Y. Li and Y. Wu, *J. Mater. Chem. C*, 2015, **3**, 11406-11411.